Journal of Thermal Biology 110 (2022) 103370

Contents lists available at ScienceDirect

Journal of Thermal Biology

journal homepage: www.elsevier.com/locate/jtherbio

Development of AI classification model for angiosome-wise interpretive substantiation of *plantar feet thermal asymmetry* in type 2 diabetic subjects using infrared thermograms

Christy Evangeline N [a,*], S. Srinivasan [a], E. Suresh [b]

[a] *Anna University – MIT Campus, Department of Instrumentation Engineering, Chennai, India*
[b] *Government Kilpauk Medical College Hospital, Department of Diabetology, Chennai, India*

ARTICLE INFO

Keywords:
Artificial intelligence
Diabetic foot syndrome
Feature extraction
Hotspot identification
Infrared thermogram

ABSTRACT

Diabetic Foot Syndrome (DFS) is the prime impetus for most of the lower extremity complications among the diabetic subjects. DFS is characterized by aberrant variations in plantar foot temperature distribution while healthy subjects exhibit a symmetric thermal pattern between the contralateral and ipsilateral plantar feet. Thus, "asymmetry analysis" of foot thermal distribution is contributory in assessment of overall foot health of diabetic subjects. The study, aims to classify symmetric and asymmetric foot regions angiosome-wise, by comparing minimal number of color image features - color moments and Dissimilarity Index. Further, the asymmetric foot regions are assessed for identifying the hotspots within such angiosomes of the patients that characterize the possibility of onset of diabetic foot ulcer. The color feature based machine learning model developed, achieved an accuracy of 98% for a 10-fold cross validation, test accuracy of 96.07% and 0.96 F1-score thereby convincing that the chosen features are amplest and conducive in the asymmetry analysis. The developed model was validated for generalization by testing on a public benchmark dataset, in which the model achieved 92.5% accuracy and 0.91 F1 score.

1. Introduction

Diabetes Mellitus, a chronic metabolic disorder, in conjunction with itself, has multifaceted complications, whose furtherance can cause ulceration in a diabetic foot. Diabetic Foot Syndrome (DFS) is one among the complications which may end up in amputations and lifelong disabilities. On these grounds, early detection and prevention of such foot ulcers becomes crucial for all diabetic subjects so much so, the World Health Organization and International Diabetes Federation have set their mission to cut down the rates of amputations due to diabetic foot by 50% (Bakker et al., 2011). Homosapiens or human beings, as we are called, are homeotherms that have the ability to maintain a consistent internal body temperature regardless of the temperature change in the ambience. The thermal regulation by loss of heat or production of heat may be altered by various pathological conditions. In cases of subjects with diabetes, the variations in plantar foot temperatures can be due to factors like peripheral arterial disease, neuropathy or neuroischemia or their combinations (Gatt et al., 2018). The infrared (IR) technology facilitates the capture of this natural heat radiation from our body as any object/body having a temperature above the absolute temperature (0K) is said to emit IR radiations. Although IR radiations cannot be perceived by naked human eyes, they can be converted to a visual image with the help of IR camera that maps the thermal variations on the surface of the skin. The quantitative and qualitative characterization of these temperature distributions helps in detecting the differences between healthy and at-risk feet. The reasoning of anomalously warmer temperature condition called hyperthermia provides an indirect evaluation method of peripheral neural health and vascular conditions of the feet of diabetic subjects among who the impaired nerve conduction and blood circulation result in loss of sensation and reduced blood perfusion (Hernandez-Contreras and Peregrina-Barreto, 2017). Hyperthermia characterized by a temperature difference of $\geq$2.2 °C between the contra lateral and ipsilateral feet is considered a manifestation of onset of diabetic foot ulcers (Benbow et al., 1994).

The foot temperature distribution patterns play a vital role in discriminating normal and abnormal feet. An aiding study performed on the thermographic foot temperature patterns of healthy individuals revealed that the skin temperature measurements by thermal camera are

* Corresponding author.
E-mail address: christy.evangeline@gmail.com (C. Evangeline N).

https://doi.org/10.1016/j.jtherbio.2022.103370
Received 1 February 2022; Received in revised form 1 October 2022; Accepted 6 October 2022
Available online 9 October 2022

feasible and reproducible and there is a similar temperature patterns between the contralateral and ipsilateral feet of healthy adults (Gatt et al., 2015) which forms an instrumental basis for further researches on diabetic foot anomalies. Depending on the severity of nerve damage, the diabetic subjects perceive loss of sensation in their lower limb which is a condition referred to as the diabetic peripheral neuropathy. Thus progressive loss of sensation in plantar foot combined with unusually high temperatures manifest the onset of foot ulceration according to Bharara et al. (2006) Yet another study performed between diabetic subjects having local complications (like callus, neuropathic ulcers) and diffuse complications (like ischemia, Charcot's foot) show temperature differences of more than 2 °C at the regions of interest (RoI) and mean temperature difference of more than 3 °C which is a convincing indication that thermal cameras are capable of discriminating between feet of diabetic subjects having no, local or diffuse foot complications (van Netten et al., 2013).

The international committee deputed by American Diabetes Association and European Association for Study of Diabetes along with International Diabetes Federation suggested HbA1c as the diagnostic test for diabetes (≥6.5% HbA1c concludes diabetes in subjects) (American Diabetes Association, 2011; Mohan et al., 2010). Based on this citation Sivanandam et al. (2012) worked using infrared imaging technology to determine foot temperature distribution in diabetic subjects versus control group and concluded that the foot temperature is negatively correlated with HbA1c value. Gatt et al. (2018) studied the temperature differences in the feet of healthy adults in relation to diabetic subjects with all possible categories of complications like healthy foot, healthy foot with diabetes, neuropathy, neuroischemia and arterial disease using medical thermography. Based on this study, it is connotatively understood that any abnormal change in foot temperature does not always indicate an immediate outbreak of ulcer, but simply the development of conditions like neuropathy, neuroischaemia and arterial disease. This helps in suggesting medical thermography to be used in early detection, prevention and management of diabetic foot syndrome.

As Artificial Intelligence (AI) techniques have an extensive ability to anatomize the images and examine in great details, its application in analysis of thermal images exhibits ample scope. The extraction of thermal foot images (RoI) from the background by unsupervised learning techniques like k-means clustering and Expectation Maximization (EM) clustering was implemented by Liu et al. (2015) to obtain patient specific image registration by attaining a sensitivity and specificity of 97.8% and 98.4% respectively. Saminathan et al. (2020), studied the symmetricity between contralateral and ipsilateral feet by using 12 gray-level and 2 temperature features from 11 RoIs in each foot and achieved 95.6% classification accuracy using Support Vector Machine (SVM) algorithm. Israel Cruz-Vega et al. (2020), developed a Deep learning network Diabetic Foot Thermogram Net (DFTNet) to classify between normal and diabetic foot with 85.3% accuracy and 91.6% sensitivity. Aside from mentioned and similar applications of AI in foot health analysis, there are various challenges in developing an automatic system in detection of diabetic foot complications (Liu et al., 2015 and Vardasca et al., 2012), hence the AI, in this sphere proves to show a vast scope for expansion.

The proposed semi-automated foot health analysis uses non-contact infrared thermographic image of plantar diabetic feet, defined by a set of minimal number of features that contribute towards asymmetry analysis based on the comparison of various Machine Learning algorithms – Random Forest, Support Vector Machine, Logistic Regression, Gaussian Naïve Bayes and k-NN classifiers. As the thermal distribution of the plantar feet is characterized and visualized by color distribution patterns in the thermal images, as a step-forward contribution, an attempt is made to study the color features in the thermal image which can largely be affected by the thermal distribution pattern. Further, the proposed system also identifies the hotspots in the asymmetric angiosome which are prone to ulcer development, by using clinically significant temperature values. The model developed was also independently tested on a public benchmark database, to assess the generalization of the model. Also, the comparison between Mean Foot Temperature, Mean Angiosome Temperature and Hotspot Temperature provides a rationale to adopt angiosome-wise comparison of the foot over comparison of the foot as a whole.

2. Materials and methods

2.1. Volunteer recruitment

This is a cross-sectional study performed on 153 diabetic subjects with >2 years of known diabetic history recruited by the diabetologists at the Dr Ambedkar Institute for Diabetes, Government Kilpauk Medical College Hospital, Chennai, India, following the clearance from the Institutional Ethics Committee. Table 1 lists the basic statistics of the study population from which the thermal data collection was done after an informed consent from every subject and by following the inclusion and exclusion criteria as in sections 2.1.1 and 2.1.2. Subsequent to recruitment of the volunteers for the study, the thermograph was acquired which was further divided into angiosome pairs and processed to fetch meaningful information - the features. The features were then input to the AI model tuned in for our application to perform the classification.

2.1.1. Inclusion criteria

Subjects with/who are:

- ≥ 2 years of diabetic history (Diabetes mellitus – type 2)
- aged between 20 and 60 years

2.1.2. Exclusion criteria

Subjects with/who are:

- visible skin changes in the plantar feet
- previous history of ulcers and/or amputations
- pediatric, neonatal and geriatric
- walking disabilities
- pregnant women

2.2. Thermal image acquisition and foreground segmentation

Fig. 1 illustrates the plantar thermal image acquisition process wherein the patients were first made to rest barefooted in supine position for 15 min, and were forborne from touching their feet, folding or crossing their legs. The 15 min duration is to enable the blood redistribution from the lower extremity to the heart through venous return thereby settling to a thermal steady state so as to achieve thermal equilibrium (Sun et al., 2005) in the feet region. The Fluke TiX580 camera having a focal plane array with 640 × 480 detectors and NETD (Noise Equivalent Temperature Difference) of 50 mK was employed in acquisition of thermal images of plantar feet, which had a spatial resolution of 640 × 480 each. The camera was mounted on a tripod and placed at a distance of approximately 0.45m from the subjects. The emissivity (of human body) was set at 0.98 (Fluke, 2021) and the humidity and ambient temperature of the room were monitored for each

Table 1
Survey and elemental statistics of the study population.

S No	Criteria	Population details
1	No. of diabetic subjects	153
2	Female subjects	93
3	Male subjects	60
4	Mean age ±SD	52.8 ± 6.8 years
5	Mean years of diabetic history	10.1 ± 5.2 years
6	Mean BMI	28.2 ± 3.9 kg/m^3

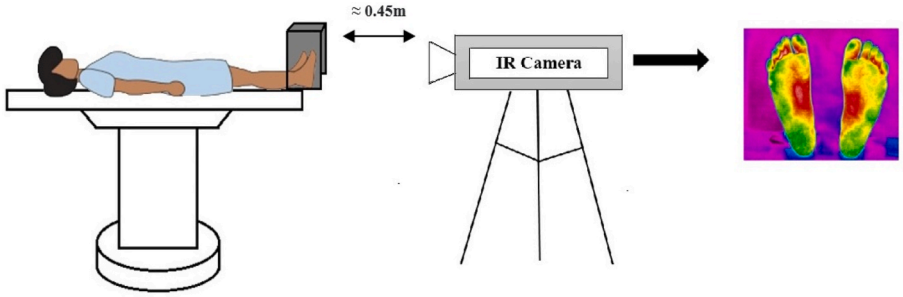

Fig. 1. Illustration of plantar feet thermal image acquisition.

study as they prove to contribute towards proper measurement of temperature (FLIR, 2016) in the field of view (FoV). A uniform black cardboard box was set to cover the 4 sides – top, right, left and behind (with provision to insert feet up till ankle) to ensure a consistent background while acquiring the plantar foot thermal image. The images were acquired using the high contrast palette of the thermal camera, as the color distinctiveness of the palette can be more informative about the small variations in the temperature distribution than monochromatic gray scale images. The foreground segmentation by removal of redundant background information, was done by performing micro contrast enhancement on the grayscale image of plantar foot followed by canny edge detection. The resultant binary image was used as a mask to burn onto the RGB thermal image in order to segment the foreground. Fig. 2 shows the step-wise output of the segmentation technique followed.

2.3. Noises in thermal images

With respect to thermal noise – according to Budzan and Wyżgolik (2014), if images are acquired outdoors, there can be a large temperature differences within the FoV, hence, there occurs Gaussian noise in thermal images. As the data acquisition for this study was performed indoors, in hospital environment, noise from the surrounding as in high temperature variations within FoV were avoided. Also the background setup will avoid interferences from the surroundings and other body parts of the subject himself/herself.

Concerning the Fixed Pattern Noise (Högasten et al., 2012) the thermal camera (Fluke Tix580) has the optomechanic shutter setup for correcting the non-uniformity caused by FPN. Hence, occurrence of FPN was ruled out in the setup.

Atmospheric noise – as according to Qiao et al. (2015) interferences from ambient sources like sun light, florescent bulbs can contribute towards inaccurate readings of target temperature. In our setup, such noise contributors like IR remote controls, IR scanners etc., were carefully kept out of the surroundings. It is also taken care that there is no external light source like florescent bulbs, doors or windows that could interfere in image acquisition.

Poisson Noise – according to Usamentiaga et al. (2014), when two objects with same temperature but with different emissivity are within the same FoV, the object with lesser emissivity will be calculated to be having lesser temperature than its counterpart object, which imposes error in measurement. But, in case of our image acquisition protocol, it was ensured that only the feet of subjects is in the FoV and also the emissivity of the target was known and set while acquiring the images. Further, the ambient temperature is set on the camera, so that the camera's software compensates for the ambient temperature effect. Thus possibilities of Poisson noise were also prevented.

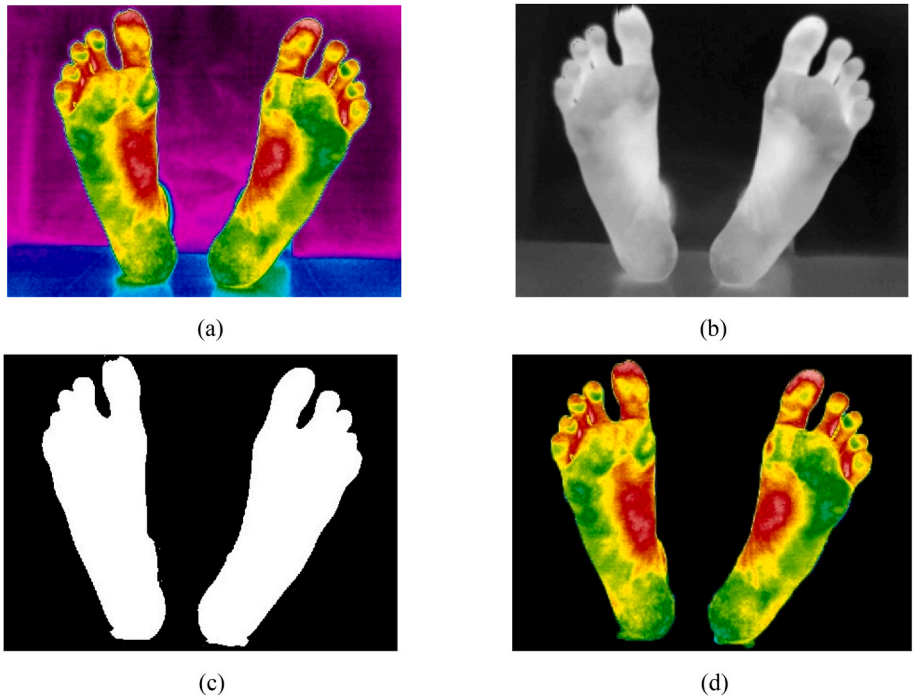

Fig. 2. Segmentation of plantar foot region from the background a) input image with background b) micro-contrast enhanced gray image c) binary mask generated post edge detection b) foreground segmented output image.

2.4. Image processing and feature extraction

Kerry Rodden et al. (2000) suggest that apportioning the images into segments or sub regions can contribute towards better quantification of the similarity/dissimilarity between each region. The entire plantar foot was separated into four angiosome regions (Fig. 3a) based on four arteries that supply to the plantar foot, namely: Medial Plantar Artery (MPA), Lateral Plantar Artery (LPA), Medial Calcaneal Artery (MCA) and Lateral Calcaneal Artery (LCA), which is shown in Fig. 3b. Understanding the four plantar foot angiosomes, proves to be useful in distinguishing the blood perfusion levels between them (Attinger et al., 2006) which in turn is utilized to assess the foot temperature distribution (Carabott et al., 2021). In this study, from the acquired plantar foot thermal image each individual angiosome pair was considered and were further contrasted into its constituent matrices from which the color image features were extracted viz. – Dissimilarity Index, and color moments - mean, variance, skewness, kurtosis. Extracting the thermal features turned out to be a cumbersome and time-consuming task, as most commercial thermal cameras does not allow accessing or overwriting of the images on platforms other their proprietary software. In such case, removal of the redundant background information cannot be done precisely, as fetching the coordinates of the background pixels is laborious and time consuming. Also, the feature extraction from thermal images could not be automated, and it has to be extracted manually from individual thermal images. This in turn can cause errors in the features extracted. Though the color patterns aren't direct representation of diabetic foot conditions, it has to be noted that the distribution of the color in the thermal image are analogous to the distribution of temperature in the FoV. Therefore, mining the features of the thermal images exported as color images can be considered to individuate the thermal distribution of the RoIs. Hence, the features - Dissimilarity Index and color moments of each pair of angiosome from ipsilateral and contralateral feet were obtained from the color images. Also, in this study, background removal and color feature extractions were automated.

2.4.1. Dissimilarity Index

The dissimilarity matrix is one of the approaches used in template matching in pattern recognition, where in the objects that have small difference with respect to the reference are labelled to be of the same class as that of the reference. Being similar to that of the nearest neighbor rule (Pekalska and Duin, 2005), the dissimilarity matrix between two images is generated by computing bin-wise Euclidean distance between the histograms of the constituent matrices (R, G and B) that yields a scalar measure of dissimilarity – the Dissimilarity Index (DI).

The DI was computed (Eqn. (1)) by comparing the histograms (h) of the same angiosome regions of the contralateral (I_ρ) and ipsilateral foot (I_λ), whose bin values (β) fall within a range (1, 256) (in case of an 8-bit image).

$$\boldsymbol{DI}(\boldsymbol{I}_\rho, \boldsymbol{I}_\lambda) = \sum_{\beta=1}^{n} \sqrt{[\boldsymbol{h}_\rho(\boldsymbol{\beta}) - \boldsymbol{h}_\lambda(\boldsymbol{\beta})]^2} \tag{1}$$

The similarity between images decreased linearly with respect to the upsurge in the DI. Notably, in thermal images, the temperature distribution from hottest to the coldest spots in the FoV is represented by a set of colors in the order, red, yellow green, light blue, dark blue and purple, making the temperature asymmetry between the feet apprehensible by considering the variations in the combination of the representative colors. Thus, DI can be considered as one of the features that can be evincive of temperature anomalies in the plantar feet. The DI of the R, G and B matrices is compared to find the maximum value amongst the three which is then considered as the DI feature of the image pair.

2.4.2. Color moments

Color moments are the statistical distribution properties of an image, used as pre-computed features for content-based image retrieval applications as they are a measure of color similarity/dissimilarity between images. Mean represents the average color value of the image, while variance, the second central moment explains the spread of intensity values around the mean – both having an immediate discernible relativity with the visual properties of the image (Gonzalez and Woods, 2018).

Skewness and kurtosis are the third and fourth order central moments describing asymmetry in the distribution and flatness of distribution peak respectively. The color moment features, the mean, variance, skewness and kurtosis were computed from the constituent matrices (M x N x 3) of contralateral and ipsilateral angiosome images (I) as follows:

$$\boldsymbol{Mean}, \boldsymbol{\mu_I} = \frac{1}{\boldsymbol{M} \times \boldsymbol{N}} \sum_{x=1}^{M} \sum_{y=1}^{N} \boldsymbol{I}(\boldsymbol{x}, \boldsymbol{y}) \tag{2}$$

$$\boldsymbol{Variance}, \boldsymbol{\sigma_1^2} = \frac{1}{\mathbf{M} \times \mathbf{N}} \sum_{x=1}^{M} \sum_{y=1}^{N} [\mathbf{1}\,(\mathbf{x}, \mathbf{y}) - \boldsymbol{\mu}_1]^2 \tag{3}$$

$$\boldsymbol{Skewness}, \boldsymbol{s_I} = \frac{1}{\boldsymbol{M} \times \boldsymbol{N}} \sum_{x=1}^{M} \sum_{y=1}^{N} \left(\frac{\boldsymbol{I}(\boldsymbol{x}, \boldsymbol{y}) - \boldsymbol{\mu_I}}{\boldsymbol{\sigma_I}} \right)^3 \tag{4}$$

$$\boldsymbol{Kurtosis}, \boldsymbol{k_I} = -\frac{1}{\boldsymbol{M} \times \boldsymbol{N}} \sum_{x=1}^{M} \sum_{y=1}^{N} \left(\frac{\boldsymbol{I}(\boldsymbol{x}, \boldsymbol{y}) - \boldsymbol{\mu_I}}{\boldsymbol{\sigma_I}} \right)^4 - \mathbf{3} \tag{5}$$

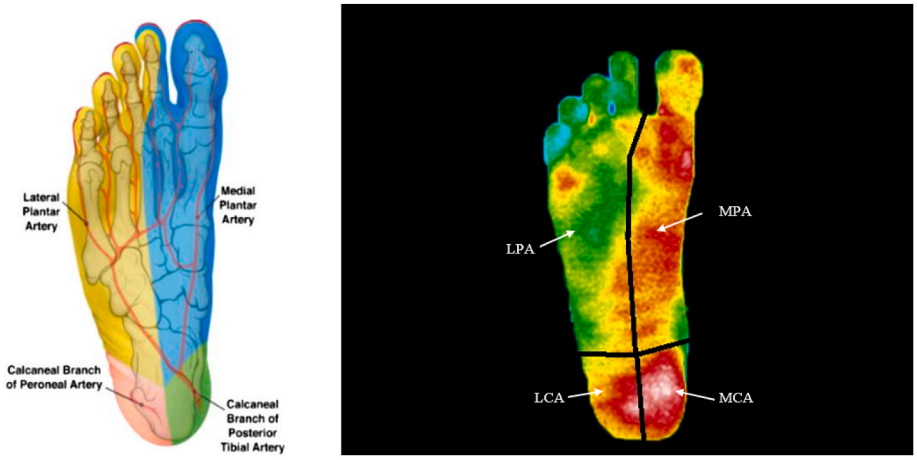

Fig. 3. a) Plantar foot angiosome anatomy (Attinger et al., 2006) **b)** Thermal Image – Angiosome wise.

Thus, including one Dissimilarity Index for each pair of angiosome and four color moments for the three constituent matrices of each angiosome, a total of 25 features were extracted from the thermal image of each subject.

2.5. Machine learning for asymmetry analysis

To classify the angiosomes as symmetric or asymmetric, a total of five machine learning algorithms were compared for maximum accuracy with minimum number of chosen features. The features were input to the algorithms – SVM, k-nearest neighbor, Gaussian Naïve Bayes, Random Forest and Logistic Regression, to adjudge which model performs judiciously for the proposed application. The entire data was split into 67%–33% proportion to be given as train-test input to the classification algorithms. The hyperparameter optimization for all the algorithms was done using 5 fold CV GridSearch technique.

SVM is a supervised learning algorithm which performs classification by constructing hyper planes which is required to be at maximum distance from the nearest training data point (support vector) and is represented as a set of points that satisfy Eqn. 6

$$\mathbf{W^T X} + b = \mathbf{0} \tag{6}$$

where w is the vector normal to the best fit hyper plane, X, the input vector and b the bias. However, unlike SVM, the distance-based model – k-nearest neighbor (k-NN) considers every point on the training set for classification of whom the choice of number of neighbors to participate in computation and the metric for computing the distance between the data points played a crucial role in improving the classification accuracy. The exponent in Eqn. (7) when changed represents different distance metrics like Euclidean (c = 2) and Manhattan (c = 1) distances.

$$\boldsymbol{d}\,(\mathbf{x},\mathbf{y}) = ((\mathbf{x_2}-\mathbf{x_1})^{\mathbf{c}} + (\mathbf{y_2}-\mathbf{y_1}^{\mathbf{c}}))^{\mathbf{1/c}} \tag{7}$$

The simple and versatile k-NN algorithm demonstrated better performance than SVM. Logistic Regression classifier is yet another algorithm considered for the performance comparison that delivered better accuracy than the previous models when crucial hyper parameters like – choice of solver algorithm and number of iterations for it to converge was set appropriately. Logistic Regression uses sigmoid function as best fit to perform the binary classification, which is represented by Eqn. (8):

$$y' = \frac{\mathbf{1}}{\mathbf{1}+e^{-z}} \tag{8}$$

Here, y' is the output of the model, $z = b + W_1X_1 + W_2X_2 + \ldots + W_NX_N$ where w and b are the weights and bias learned by the model while, x values are the feature values. Naïve Bayes algorithm, a probabilistic classification model that works on the basis of Bayes theorem (Eqn. (9)) was included in the comparison for asymmetry analysis.

$$\boldsymbol{P(C|X)} = \frac{\boldsymbol{P(X|c)P(C)}}{\boldsymbol{P(X)}} \tag{9}$$

The Bayes theorem calculates the posterior probability P(C|X), of the target class when the predictors are presented (X, attributes) from P(C), P(X) – the prior probability of the target and predictor and P(X|C) – probability of the predictor when the class is given. The Gaussian Naïve Bayes algorithm uses the above logic to conclude on the target of the data whose attributes/features are given.

The Random Forest model follows an ensemble technique to perform parallel learning from multiple Decision Trees, making the seldom "poor learners" come together as "potent learners". The Random Forest model coalesces the individual predictions of the constituent Decision Trees by averaging them into final prediction. There were multiple hyper parameters tuned in for the Random Forest model few of which are number of trees in the forest, depth of the trees, minimum number of samples per split and the model proved to have better performance than other algorithms implemented for the study. The hyperparameters were optimized using 5-fold CV GridSearch algorithm and the best parameters chosen by the algorithm have been tabulated in Table 2. As hyperparameters tuning is not applicable for Gaussian Naïve Bayes, the curve smoothing parameter was set at its default value.

Test and validation accuracy, F1-score, precision, recall, confusion matrix and area under the Receiver Operating Characteristics (ROC) curve were the metrics compared to interpret the performance of individual algorithms. The acronyms TP, TN, FP, FN (in Eqns. (10)–(12)) stand to represent True Positive, True Negative, False Positive and False Negative respectively. The ROC curve, as a gauge for the classifier performance, plots False Positive Rate (FPR) versus True Positive Rate (TPR) and higher the Area Under the ROC Curve (AUC), better is the model's performance.

$$\boldsymbol{Accuracy} = \frac{\boldsymbol{TP}+\boldsymbol{TN}}{\boldsymbol{TP}+\boldsymbol{TN}+\boldsymbol{FP}+\boldsymbol{FN}} \tag{10}$$

$$\boldsymbol{Precision} = \frac{\boldsymbol{TP}}{\boldsymbol{TP}+\boldsymbol{FP}} \tag{11}$$

$$\boldsymbol{Recall} = \frac{\boldsymbol{TP}}{\boldsymbol{TP}+\boldsymbol{FN}} \tag{12}$$

$$\boldsymbol{F1\ Score} = \mathbf{2} \times \frac{(\boldsymbol{Precision} \times \boldsymbol{Recall})}{(\boldsymbol{Precision} + \boldsymbol{Recall})} \tag{13}$$

$$\boldsymbol{TPR} = \frac{\boldsymbol{TP}}{\boldsymbol{TP}+\boldsymbol{FN}} \tag{14}$$

$$\boldsymbol{FPR} = \frac{\boldsymbol{FP}}{\boldsymbol{FP}+\boldsymbol{TN}} \tag{15}$$

3. Results

In this study, a total of 153 subjects with 612 pairs of angiosome regions were included for the analysis. The angiosome image categorization into "symmetric" and "asymmetric" was performed based on the diabetologists' endorsement and also attributed by the mean temperature difference of ≥1 °C between the corresponding angiosomes (Vilcahuaman et al., 2014). Fig. 4 a and b shows the 3-D thermal profile of right and left foot of a normal and a diabetic condition respectively. The normal feet in Fig. 4 a, have a higher temperature in the arch of the foot region than other regions of the foot, while diabetic feet have an irregular distribution of temperature patterns as shown in Fig. 4 b. Even though the temperature range or mean foot temperature vary from subject to subject, the thermal pattern follows a similar, symmetric trend in normal subjects in contrast to an irregular trend in diabetic subjects.

After contrasting the foot image into angiosome-wise regions, it was proceeded to further categorize each region to be symmetric or asymmetric on comparison with the contralateral foot, based on the features extracted. Table 3 holds the descriptive statistics like minimum difference, maximum difference and mean value with the Standard Deviation (SD) of the Dissimilarity Index between the angiosome pairs. It is to be noted that the range value (maximum – minimum) as well as the mean

Table 2
Optimized hyperparameters.

S No	Algorithms	Hyperparameters
1	SVM	C = 1.0, kernel = 'rbf',gamma = 'scale'
2	k-NN	n_neighbors = 7, weights = "distance"
3	Gaussian Naïve Bayes	var_smoothing = 1e-09
4	Random Forest	n_estimators = 250, max_depth = 5, min_samples_split = 2, min_samples_leaf = 1,max_fetaures = "auto", bootstrap = True
5	Logistic Regression	max_iter = 800, solver = "lbfgs"

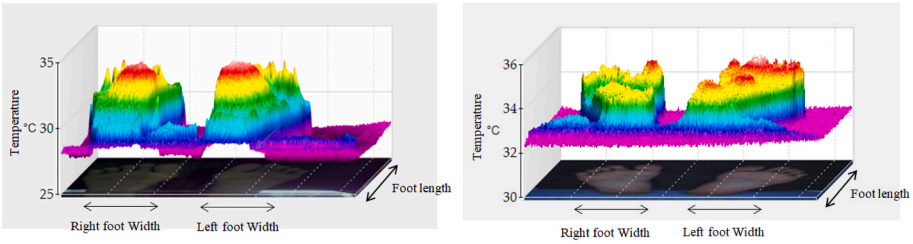

Fig. 4. a) 3-D plot of thermal profile of normal subjects **b)** 3-D plot of thermal profile of diabetic subjects.

Table 3
Dissimilarity index – angiosome-wise.

S No	Region	Minimum DI value	Maximum DI value	Mean ± SD of the DI value
1	MPA region	423	11334	3367 ± 1832
2	LPA region	808	14543	4048 ± 2482
3	MCA region	299	6175	1623 ± 871
4	LCA region	264	3813	1610 ± 778

and SD values vary according to the area covered by each angiosome. The angiosome that covers more area than others have a higher mean, SD and range values comparatively, in line with which the values are greater for the LPA region than MPA, MCA and LCA regions falling in order. Tables 4 and 5 carry the descriptive statistics of the angiosome-wise color moments of the constituent matrices.

Considering a sample size of 110 from the entire population, Tables 6 and 7 represent the interval estimate of mean values of the color moment features of true population for all the angiosomes, with 95% Confidence Interval (CI). While the p-values provide evidence to reject the null hypothesis and show statistical significance or non-significance between groups, the CI provides the estimate of such difference between the groups. According to Tan and Tan (2010) if the 95% CI for the difference between the two groups contains value 0, this means that the p-value is > 0.05 and contrarily if it does not contain value 0, then the p-value is < 0.05. Therefore, referring to estimate of the mean interval in Tables 6 and 7, the p value is < 0.05 – thereby rejecting the null hypothesis.

The features were input to machine learning algorithms – SVM, k-nearest neighbor, Gaussian Naïve Bayes, Random Forest and Logistic Regression, amongst which the Random Forest model showed to achieve a maximum test accuracy of 96.07%, 30 times 10-fold cross validation accuracy of 98% (±0.043) and also a higher F1 score of 0.96 than other machine learning models employed. While accuracy measured the correct predictions, F1 score included the incorrect classifications while measuring the performance of each model. Though the confusion matrix of SVM and k-NN show a higher TP for class "Asymmetric", their classification into class "Symmetric" shows to be poor, that is smaller TN, with more misclassifications as FN (Table 8). However, the Random Forest model, showed the best classification performance amongst the models employed, which is shown in Fig. 5.

The area under the ROC curve is another performance measure that computes the model's degree of separability between the classes. As the ROC curve itself is the probability curve that plots False Positive Rate vs True Positive Rate, it is the most common way to visualize the performance of a classifier with two output classes. By and large an AUC value of 0.5, submits no discrimination between the classes while a value between 0.7 and 0.8 are considered acceptable. The AUC value from 0.8 to 0.9 is regarded excellent and the value above 0.9 is outstanding for a classifier (Hosmer and Lemeshow, 2000). Amongst the algorithms employed, AUC was maximum for the Random Forest model, proving that the tuned-in model showed the best discrimination between classes.

Similarly, precision and recall are other measures to predict the success of the model. Though precision for class "Asymmetric" is maximum for k-NN, SVM and Random Forest, the precision for the class "Symmetric" is comparatively higher for Random Forest model. Likewise, recall for class "Asymmetric" is higher for Random Forest and Gaussian Naïve Bayes, however between the two, recall for class "Symmetric" is at its maximum value 1, for Random Forest (Fig. 6 a and b).

In order to substantiate the performance of the developed color feature based classification model, an independent test on a public domain database (Hernández-Contreras et al., 2019) was carried out. The database comprised of both control and diabetic subjects' data (DM). To have a comparative performance test, DM dataset is considered. This dataset included 122 thermal profiles and color images of thermal distribution in plantar feet as.csv and.png files respectively. Each patient data included images of full foot as well as images of all 4 angiosomes with their corresponding thermal profile.

Out of 122, 40 patient data were taken up for the performance evaluation of the model. First 40 subjects in the database were chosen in order that any odds of bias in subject selection was ruled out. By automated feature extraction process, the color image features were extracted from the angiosome images in the database. Alongside, the Mean Angiosome Temperature (MAT) values were extracted from the corresponding temperature files. The target for this test set was labelled

Table 4
Color moments – Mean and Variance – Minimum, maximum, average and standard deviation of R, G, B matrices.

S No	Region	Mean min-max values (Average ± SD)			Variance min-max values (Average ± SD)		
		R	G	B	R	G	B
1	MPA region	0.57–16.05 (7.67 ± 3.7)	1.38–14.85 (9.27 ± 2.5)	0.4–12.93 (4.35 ± 3.5)	13.5–3177.6 (1441.6 ± 802.4)	102.9–2848.1 (1614.4 ± 504)	6.72–2667 (748.2 ± 736)
2	LPA region	0.15–19.45 (7.68 ± 4.6)	0.34–17.5 (10.74 ± 3.8)	0.5–21.8 (8.6 ± 6)	3.32–4021.2 (1349.7 ± 950.3)	7.06–3088.2 (1847.1 ± 699.2)	9.15–4322.2 (1571.7 ± 1243.6)
3	MCA region	0.07–6.99 (2.01 ± 1.5)	0.37–5.14 (2.76 ± 0.91)	0.09–15.37 (1.16 ± 1.67)	0.59–1237.2 (378.6 ± 332.1)	23.12–1018.4 (494.9 ± 208.1)	1.29–3115.2 (195.2 ± 356.7)
4	LCA region	0.07–5.65 (1.92 ± 1.6)	0.09–5.99 (2.92 ± 1.06)	0.12–5.56 (1.34 ± 1.45)	0.62–1287.3 (353.8 ± 350)	0.95–1101.5 (524 ± 236)	1.89–1144.2 (231.3 ± 314.5)

Table 5
Color moments – Skewness and Kurtosis – Minimum, maximum, average and standard deviation of R, G, B matrices.

S No	Region	Skewness min-max values (Average ± SD)			Kurtosis min-max values (Average ± SD)		
		R	G	B	R	G	B
1	MPA region	0.23–0.88 (0.35 ± 0.11)	0.22–0.56 (0.27 ± 0.04)	0.25–1.13 (0.5 ± 0.2)	0.05–0.49 (0.12 ± 0.07)	0.05–0.27 (0.07 ± 0.02)	0.06–0.8 (0.22 ± 0.16)
2	LPA region	0.26–1.61 (0.35 ± 0.14)	0.197–1.94 (0.28 ± 0.15)	0.197–1.02 (0.37 ± 0.18)	0.04–1.67 (0.12 ± 0.13)	0.04–2.06 (0.09 ± 0.16)	0.04–0.61 (0.31 ± 0.11)
3	MCA region	0.33–3.97 (0.82 ± 0.55)	0.36–0.95 (0.5 ± 0.07)	0.23–2.36 (0.99 ± 0.47)	0.10–7.92 (0.67 ± 0.92)	0.13–0.81 (0.25 ± 0.08)	0.05–3.24 (0.84 ± 0.65)
4	LCA region	0.39–3.8 (0.88 ± 0.59)	3.34–3.57 (0.51 ± 0.26)	0.38–1.93 (0.9 ± 0.4)	0.15–6.95 (0.76 ± 0.92)	0.12–6.98 (0.28 ± 0.55)	0.14–2.21 (0.69 ± 0.49)

Table 6
Mean interval estimate of the true population of 1st and 2nd order color moments – based on 95% Confidence Interval.

S No	Region	Mean			Variance		
		R	G	B	R	G	B
1	MPA region	[6.96, 8.34]	[8.8, 9.74]	[3.7, 5]	[1290, 1590]	[1520, 1710]	[610, 886]
2	LPA region	[6.82, 8.54]	[10, 11.4]	[7.48, 9.72]	[1170, 1530]	[1720, 1980]	[1340, 1800]
3	MCA region	[1.73, 2.29]	[2.59, 2.93]	[0.85, 1.47]	[317, 441]	[456, 534]	[129, 262]
4	LCA region	[1.62, 2.22]	[2.72, 3.12]	[1.07, 1.61]	[288, 419]	[480, 568]	[173, 290]

following the same procedure as used to categorize the real time data, that is, if the MAT difference was ≥1 °C, then the angiosomes were labelled to be "asymmetric" and labelled "symmetric" if otherwise. The features extracted from the benchmark database were then input as a test set to the Random Forest model trained on the real time data features. The model was able to achieve a test accuracy of 92.5% and F1 score of 0.91 on the independent test performed on the public benchmark dataset. Table 9 tabulates the performance metrics of the model on the public domain database.

Table 10 tabulates the consolidated number of subjects within combinations of classes that materialized among 4 angiosome regions. With the average years of diabetic history of 153 subjects being 10.1 ± 5.2, 26.14% of the population had asymmetry in (any) 3 angiosomes and symmetry in 1 angiosome, while subjects with asymmetry in all four angiosomes were 35.9% and other subjects had at least 2 symmetric angiosomes.

As the next step, in each asymmetric angiosome classified by the model, the presence of hotspots (characterized by a temperature difference of 2.2 °C or more) were identified if any, which is considered as a prognostic indicator of possible ulcer onset (Benbow et al., 1994). Fig. 7 a represents thermal image of a diabetic subject for whom the LPA, MCA and LCA regions were classified to be asymmetric and based on thermal profile the MPA region was found to have a hotspot region with 2.7 °C difference, while other 2 regions had a difference of 1.1 °C and 1 °C respectively. Similarly, Fig. 7 b, c and d show subjects with hotspots in LPA, MCA and LCA angiosome regions with a temperature difference of 4.1 °C, 2.7 °C and 2.5 °C respectively from their contralateral angiosome regions. Therefore, when perusing through the thermal image pixel-wise, to identify hotspot regions is burdensome, prior classification into asymmetric or symmetric angiosome pairs and then proceeding to scrutinize only through the asymmetric region to narrow down to hotspot region tails out the tedious process.

Table 11 holds the comparison between the Mean (plantar) Foot Temperature (MFT), Mean Angiosome Temperature (MAT) and Hotspot temperature (HT). It is to be noted that the comparison has been performed only among subjects that had hotspots in the respective

Table 8
Performance metrics of the employed algorithms.

S No	Algorithm	F1 score	Test accuracy	30 times 10 fold cross validation accuracy (SD)	Confusion matrix	AUC
1	SVM	0.81	84%	92.2% (0.125)	39 0 8 4	0.67
2	k-NN	0.86	88%	93% (0.114)	39 0 6 6	0.75
3	Gaussian Naïve Bayes	0.92	92.15%	86% (0.092)	37 2 2 10	0.89
4	Random Forest	0.96	96.07%	98% (0.043)	39 0 2 10	0.92
5	Logistic Regression	0.90	90.1%	96.1% (0.052)	37 2 3 9	0.85

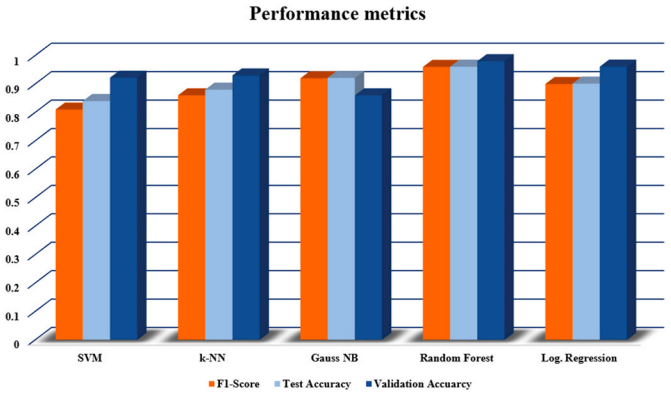

Fig. 5. Performance comparison between models - F1-score, test accuracy and validation accuracy.

Table 7
Mean interval estimate of the true population of 3rd and 4th order color moments – based on 95% Confidence Interval.

S No	Region	Skewness			Kurtosis		
		R	G	B	R	G	B
1	MPA region	[0.329, 0.371]	[0.263, 0.277]	[0.463, 0.537]	[0.107, 0.133]	[0.066, 0.074]	[0.19, 0.25]
2	LPA region	[0.324, 0.376]	[0.252, 0.308]	[0.336, 0.404]	[0.0957, 0.144]	[0.0601, 0.12]	[0.109, 0.151]
3	MCA region	[0.717, −0.923]	[0.487, 0.513]	[0.902, 1.08]	[0.498, 0.842]	[0.235, 0.265]	[0.719, 0.961]
4	LCA region	[0.77, 0.99]	[0.461, −0.559]	[0.825, 0.975]	[0.58, 0.932]	[0.177, 0.38]	[0.598, 0.782]

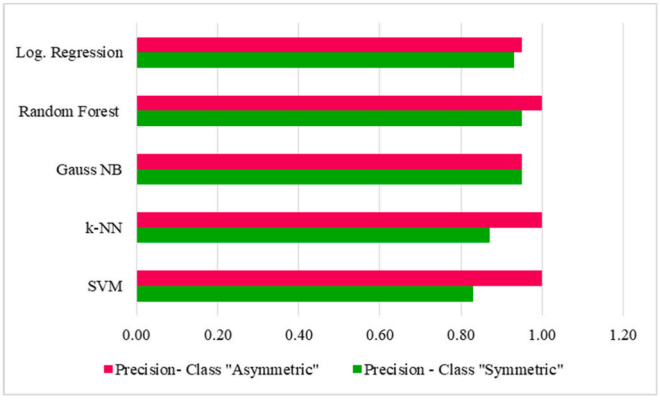

(a)

(b)

Fig. 6. a) Class-wise Precision plot **b)** Class-wise Recall plot.

Table 9
Performance of the color feature based classification model on public benchmark dataset.

S No	Performance metric	Values
1	Test Accuracy	92.5%
2	F1 Score	0.91
3	Confusion matrix	15 0 3 22

Table 10
Consolidated number of subjects within each combination of class – Angiosome-wise.

S No	MPA	LPA	MCA	LCA	No. of subjects
1	Asymmetric	Asymmetric	Asymmetric	Asymmetric	55
2	Asymmetric	Asymmetric	Symmetric	Symmetric	19
3	Asymmetric	Symmetric	Asymmetric	Asymmetric	4
4	Asymmetric	Asymmetric	Asymmetric	Symmetric	15
5	Asymmetric	Asymmetric	Symmetric	Asymmetric	13
6	Asymmetric	Symmetric	Symmetric	Asymmetric	3
7	Asymmetric	Symmetric	Symmetric	Symmetric	11
8	Asymmetric	Symmetric	Asymmetric	Symmetric	6
9	Symmetric	Asymmetric	Symmetric	Symmetric	2
10	Symmetric	Asymmetric	Asymmetric	Asymmetric	8
11	Symmetric	Asymmetric	Symmetric	Asymmetric	3
12	Symmetric	Asymmetric	Asymmetric	Symmetric	2
13	Symmetric	Asymmetric	Symmetric	Symmetric	4
14	Symmetric	Symmetric	Asymmetric	Asymmetric	3
15	Symmetric	Symmetric	Symmetric	Asymmetric	1
16	Symmetric	Symmetric	Symmetric	Symmetric	4

angiosomes. Though the subjects had hotspot regions in one of the feet, not much of the temperature difference gets reflected in the MFT value or in the difference between right and left MFT. However, when the comparison is done angiosome-wise, the mean temperature of the angiosome that has a hotspot shows a conspicuously higher temperature than the MFT of the same foot. This is because when the whole plantar foot is considered for thermal analysis, the hotspot temperature gets weighed down while calculating the mean temperature, per contra, as we narrow down to the specific angiosome with the hotspot based on the proposed asymmetry analysis, the mean angiosome temperature seems to be a better reflection of the presence of hotspot region. The HT is the temperature at the specific hotspot – marked with * in Table 11, while the temperature in the corresponding left or the right column under HT holds the temperature of the same regions as the hotspot in the contralateral foot. The difference in HT values is $\geq$ 2.2 °C in all angiosomes, which is indicative of an ulcer onset in the region. However, narrowing down to possible hotspot regions to perform asymmetry analysis might prove less useful. This is because, though neuropathic ulcers mostly occur in pressure point areas in the plantar aspect of the foot, neuro-ischemic foot ulcers can occur anywhere along the edges of the foot or on the medial surface of metatarsophalangeal joint. So, considering only the plantar foot pressure points or pre-defined points for the asymmetry analysis holds a residual uncertainty of missing out on a hotspot region. Hence asymmetry analysis of angiosomes, prove to be effective for the proposed analysis.

4. Conclusion

The prime focus of this work was on developing an Artificial Intelligence model that can discriminate between symmetric and asymmetric angiosomes using minimum-possible number of features. Based on the results, it is seen that, in most diabetic subjects, when the entire foot is considered for asymmetry comparison, most of them have a tendency to fall within the class “symmetric” and the “at-risk” zones go undetected which in most cases may become detrimental. Thus, narrowing down to locate the regions of asymmetry within each foot may be the next expected level of prediction. And so, in this study angiosome-wise analysis of the thermal foot images using color image features enabled contra-distinguishing between the symmetric and asymmetric regions in specific, instead of classifying entire foot under the class “symmetric”. Thus the work involved a total of 25 features extracted from color image processing of angiosome-wise plantar feet thermal images and validating the Random Forest model exhibiting maximum 30 times 10-fold cross validation accuracy of 98% ($\pm$0.043), test accuracy of 96.07% with specificity and sensitivity of 1.00 and 0.95 respectively in asymmetry analysis of diabetic feet.

Over and above, the model was subjected to independent testing on a public benchmark dataset and showed that it generalized well with the unseen data as well. Further the model used the clinically significant thermal data to filter-out the subjects with ulcer-prone regions based on the hotspots with temperature difference of $\geq$2.2 °C. The angiosome based study approach showed to individualize the deviations in the blood perfusion, thereby being denotative of the risk of ulceration in each sub-region. The model developed, thus can be considered viable in application as a screening system among the masses in the thick of which diabetics are conspicuously high.

Author statement

Christy Evangeline N: Conceptualization, Methodology, Software, Writing – Original Draft, Formal Analysis, Data Curation. Srinivasan S: Validation, Writing – Review and Editing, Visualization. Suresh E: Investigation, Resources, Supervision.

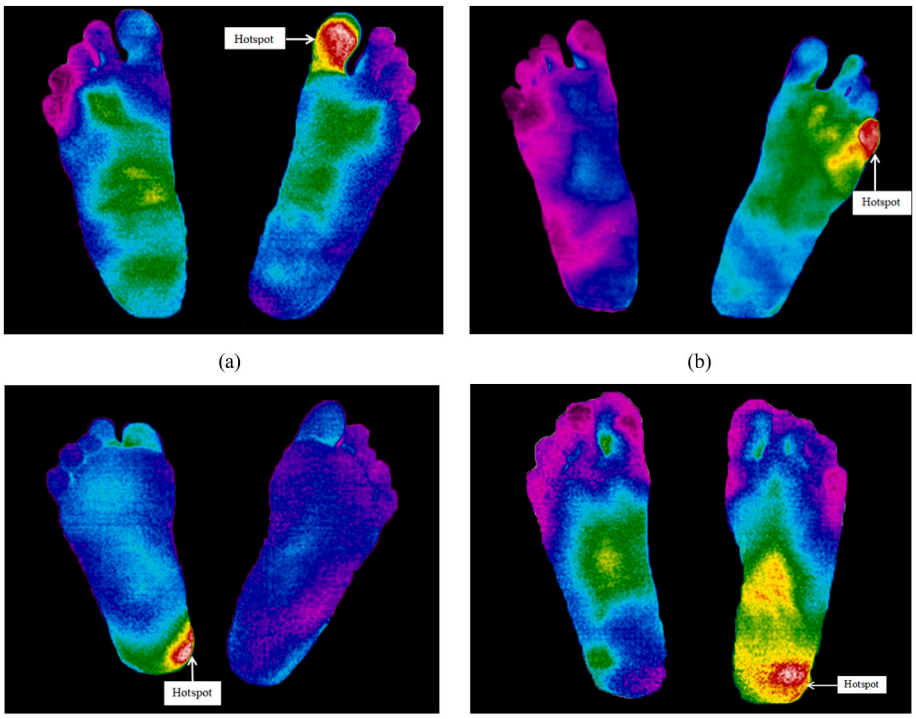

Fig. 7. Thermal image of a subject with hotspot in a) MPA angiosome b) LPA angiosome c) MCA angiosome d) LCA angiosome.

Table 11
Comparison of MFT, MAT and HT in MPA, LPA, MCA and LCA angiosomes (in °C).

S No	Subjects with hotspots	Mean Foot Temperature			Mean Angiosome Temperature			Hotspot Temperature		
		Right	Left	MFT difference	Right	Left	MAT difference	Right	Left	HT difference
MPA ANGIOSOME										
1	Patient 06	32.7	30.1	2.6	33.8	30.8	3	**34.7**[a]	30.2	4.5
2	Patient 85	32.3	33.7	1.4	32.1	34.2	2.1	32.3	**35.7**[a]	3.4
3	Patient 98	32.8	33.8	1.0	32.7	33.8	1.1	30.9	**33.4**[a]	2.5
4	Patient 139	32.8	33.7	0.9	33	34	1.0	32.1	**34.3**[a]	2.2
5	Patient 54	32.6	33.3	0.7	32.6	33.6	1.0	32	**34.2**[a]	2.2
6	Patient 35	34.3	34	0.3	34.5	32.9	1.6	**34.9**[a]	32.4	2.5
7	Patient 126	32.9	32.9	0.0	32.9	34.4	1.5	32.5	**35.2**[a]	2.7
LPA ANGIOSOME										
1	Patient 05	32.7	33.7	1.0	32.2	34.2	2.0	32.4	**35.6**[a]	3.2
2	Patient 23	33.7	32.7	1.0	33.8	30.8	3.0	**34.7**[a]	30.6	4.1
3	Patient 33	33.7	34.9	1.2	33.3	35.3	2.0	32.9	**37.0**[a]	4.1
4	Patient 17	32.8	33.7	0.9	32.7	33.7	1.0	31.6	**34**[a]	2.4
5	Patient 42	34.1	34.3	0.2	33.8	34.2	0.4	33.2	**35.4**[a]	2.2
6	Patient 136	33.2	32.7	0.5	33.1	32.4	1.3	**34.6**[a]	32.4	2.2
MCA ANGIOSOME										
1	Patient 06	32.7	30.1	2.6	34.2	31.2	3	**34.5**[a]	31.2	3.3
2	Patient 121	33.2	32.8	0.4	34.2	32.8	1.4	**35.5**[a]	32.8	2.7
3	Patient 78	30.6	30.1	0.5	31.4	30.3	1.1	**31.9**[a]	29.7	2.2
4	Patient 124	32.2	32.7	0.5	32.3	33.6	1.3	32	**34.3**[a]	2.3
LCA ANGIOSOME										
1	Patient 09	33.7	32.7	1.0	34.2	31.8	2.4	**34.5**[a]	32	2.5
2	Patient 98	32.8	33.8	1.0	32.7	33.9	1.2	32.2	**34.4**[a]	2.2
3	Patient 129	32.2	32.7	0.5	32.1	33.4	1.3	31.9	**34.1**[a]	2.2

[a] Hotspot regions

Conflict of interest

The authors declare no conflict of interest.

Funding

This research did not receive any specific grant from funding agencies in the public, commercial, or not-for-profit sectors.

Data availability

The authors are unable or have chosen not to specify which data has been used.

Acknowledgement

This work was supported by University Grants Commission (UGC),

Government of India under UGC-SAP-DRS-I project (F.5-7/2016/DRS-I (SAP-II)). We are genuinely grateful to Anna University, Chennai, India to have supported this project work by providing us with ACRF - Anna Centenary Research Fellowship. Also, we are also thankful to the participants in the study and the diabetologists at Dr. Ambedkar Institute of Diabetes, Government Kilpauk Medical College Hospital for their adept support and insightful guidance all through the data collection and data analysis process.

References

American Diabetes Association, 2011. Standards of medical care in Diabetes. Diabetes Care 34 (Suppl. 1), S11–S61. https://doi.org/10.2337/dc11-S011. Suppl 1.

Attinger, C.E., Evans, K.K., et al., 2006. Angiosomes of the foot and ankle and clinical implications for limb salvage: reconstruction, incisions, and revascularization. Plast. Reconstr. Surg. 117 (7 Suppl. l), 261S–293S. https://doi.org/10.1097/01.prs.0000222582.84385.54.

Bakker, K., Apelqvist, J., Schaper, N.C., 2011. International working group on diabetic foot editorial board. Practical guidelines on the management and prevention of the diabetic foot. Diabetes Metab Res Rev 28 (Suppl. 1), 225–231. https://doi.org/10.1002/dmrr.2253.

Benbow, S.J., Chan, A.W., et al., 1994. The prediction of diabetic neuropathic plantar foot ulceration by liquid-crystal contact thermography. Diabetes Care 17 (8), 835–839. https://doi.org/10.2337/diacare.17.8.835.

Bharara, M., Cobb, J.E., Claremont, D.J., 2006. Thermography and thermometry in the assessment of diabetic neuropathic foot: a case of furthering the role of thermal techniques. Int. J. Low. Extrem. Wounds 5 (4), 250–260. https://doi.org/10.1177/1534734606293481.

Budzan, S., Wyżgolik, R., 2014. Noise reduction in thermal images. Lect. Notes Comput. Sci. 116–123. https://doi.org/10.1007/978-3-319-11331-9_15.

Carabott, M., Formosa, C., et al., 2021. Thermographic Characteristics of the diabetic foot with peripheral arterial disease using the angiosome concept. Exp. Clin. Endocrinol. Diabetes 129 (2), 93–98. https://doi.org/10.1055/a-0838-5209.

Cruz-Vega, I., Hernandez-Contreras, D., et al., 2020. Deep learning classification for diabetic foot thermograms. Sensors 20 (6), 1762. https://doi.org/10.3390/s20061762.

Flir, 2016. FLIR-infrared Camera Accuracy and Uncertainty in Plain Language. https://www.flir.in/discover/rd-science/infrared-camera-accuracy-and-uncertainty-in-plain-language/. (Accessed 27 March 2021).

Fluke. Fluke - hotspot detection in thermal imaging. https://www.fluke.com/en-in/learn/blog/thermal-imaging/hot-spot detection. (Accessed 27 March 2021).

Gatt, A., Formosa, C., Cassar, K., et al., 2015. Thermographic patterns of the upper and lower limbs: baseline data. Int J Vasc Med, 831369. https://doi.org/10.1155/2015/831369.

Gatt, A., Falzon, O., Cassar, K., et al., 2018. Establishing differences in thermographic patterns between the various complications in diabetic foot disease. Internet J. Endocrinol. 9808295 https://doi.org/10.1155/2018/9808295.

Gonzalez, Rafael C., Woods, Richard E., 2018. Digital Image Processing, third ed. Prentice-Hall Inc., New Jersey, USA, ISBN 978-0-13-168728-8.

Hernandez-Contreras, D., Peregrina-Barreto, H., 2017. A Quantitative Index for Classification of Plantar Thermal Changes in Diabetic Foot. Infrared Physics and Technology, vol. 81. Elsevier, pp. 242–249. https://doi.org/10.1016/j.infrared.2017.01.010.

Hernández-Contreras, Daniel, Peregrina-Barreto, Hayde, Rangel-Magdaleno, Jose, Renero-Carrillo, Francisco, 2019. Plantar Thermogram database for the study of diabetic foot complications. IEEE Dataport. https://doi.org/10.21227/tm4t-9n15.

Högasten, Nicholas, et al., 2012. Non-uniformity Correction Techniques for Infrared Imaging Devices. World Intellectual Property Organization. WO 2012/170949 A2.

Hosmer, D.W., Lemeshow, S., 2000. Applied Logistic Regression, second ed. John Wiley and Sons, NY, pp. 160–164. https://doi.org/10.1002/0471722146 (Chapter 5).

Liu, C., van Netten, J.J., van Baal, J.G., et al., 2015. Automatic detection of diabetic foot complications with infrared thermography by asymmetric analysis. J. Biomed. Opt. 20 (2), 26003 https://doi.org/10.1117/1.JBO.20.2.026003.

Mohan, V., Vijayachandrika, V., et al., 2010. A1C cut points to define various glucose intolerance groups in Asian Indians. Diabetes Care 33 (3), 515–519. https://doi.org/10.2337/dc09-1694.

Pekalska, Elzbieta, Duin, Robert, 2005. The Dissimilarity Representation for Pattern Recognition: Foundations and Applications (Machine Perception and Artificial Intelligence). World Scientific Publishing Co., Inc., New Jersey, USA https://doi.org/10.1142/5965.

Qiao, S., Zhang, K., Zhang, X., Wang, H., 2015. Research of knee infrared image noise reduction and enhancement. In: International Conference on Identification, Information, and Knowledge in the Internet of Things (IIKI), pp. 305–306. https://doi.org/10.1109/IIKI.2015.73.

Rodden, Kerry, et al., 2000. A comparison of measures for visualising image similarity. Challenge of Image Retrieval.

Saminathan, J., Sasikala, M., et al., 2020. Computer aided detection of diabetic foot ulcer using asymmetry analysis of texture and temperature features. Infrared Phys. Technol. 105 https://doi.org/10.1016/j.infrared.2020.103219.

Sivanandam, S., Anburajan, M., et al., 2012. Medical Thermography: a diagnostic approach for type 2 diabetes based on non-contact infrared thermal imaging. Endocrine 42 (2), 343–351. https://doi.org/10.1007/s12020-012-9645-8.

Sun, P.C., Jao, S.H., Cheng, C.K., 2005. Assessing foot temperature using infrared thermography. Foot Ankle Int. 26 (10), 847–853. https://doi.org/10.1177/107110070502601010.

Tan, S.H., Tan, S.B., 2010. The correct interpretation of confidence intervals. Proceedings of Singapore Healthcare 19 (3), 276–278. https://doi.org/10.1177/201010581001900316.

Usamentiaga, R., Venegas, P., et al., 2014. Infrared thermography for temperature measurement and non-destructive testing. Sensors 14 (7), 12305–12348. https://doi.org/10.3390/s140712305.

van Netten, Japp J., van Baal, Jeff G., Liu, Chanjuan, 2013. Infrared thermal imaging for automated detection of diabetic foot complications. Journal of Diabetes Science and Technology 7 (5), 1122–1129. https://doi.org/10.1177/193229681300700504.

Vardasca, R., Ring, F., et al., 2012. Thermal symmetry of upper and lower extremities in healthy subjects. Thermology International 22 (2), 53–60.

Vilcahuaman, L., Harba, R., et al., 2014. Detection of diabetic foot hyperthermia by infrared imaging. In: Annu Int Conf IEEE Eng Med Biol Soc, pp. 4831–4834. https://doi.org/10.1109/EMBC.2014.6944705.